

Expressions for Resonant Frequency of Wirelessly Accessible Planar Mirrored-Coil Sensor in Biomedicine

Jongheon Lee, Hyunwoo Kim, *Student Member, IEEE*, Kun-Woo Park, Jong-Han Kim^{ID},
and Sanghoek Kim^{ID}, *Member, IEEE*

Abstract—Planar mirrored-coil structures are often used in the field of biomedicine as a sensor to measure physiological signals wirelessly. Although there are many studies on interrogation methodologies, research on the sensor itself remains understudied. In this article, we report an analytical formulation and a data-fitted formula to calculate the resonant frequency for a planar mirrored-coil sensor. Compared to the measured results, our analytical formula and data-fitted formula deviate by 13% and 9% median errors, respectively, which is much more accurate than the conventional one, 23%. It shows that both methods provide a way to quickly evaluate and design a planar mirrored-coil structure with high precision.

Index Terms—Convex optimization, method of images, passive LC sensor.

I. INTRODUCTION

LC-RESONATOR-BASED sensors are widely used to sense physiological signals for various diagnosis and health monitoring purposes. For examples, LC-resonator-based sensors have been proposed to sense blood pressure [1], intracranial pressure [2], intraocular pressure [3]–[6], and bladder pressure [7]. It consists of a planar coil(s) and a capacitance coupled with the coil, forming an LC resonance at a certain frequency ω_s . When external pressure is applied, the capacitance increases as the separation between the electrodes decreases. The increase of capacitance subsequently

Manuscript received May 15, 2021; revised July 10, 2021; accepted August 9, 2021. This work was supported in part by the National Research Foundation of Korea (NRF) under Grant NRF-2017R1C1B2009892 and Grant NRF-2018R1A6A1A03025708, in part by the Ministry of Science and ICT (MSIT), South Korea, through the Information Technology Research Center (ITRC) support program supervised by the Institute for Information and Communications Technology Planning and Evaluation (IITP) under Grant IITP-2016-0-00291-0051001 and Grant IITP-2021-0-02046, and in part by the Industrial Technology Innovation Program funded by the Ministry of Trade, Industry and Energy (MOTIE), South Korea, under Project 20002712. (Corresponding authors: Sanghoek Kim; Jong-Han Kim.)

Jongheon Lee and Sanghoek Kim are with the Department of Electronics and Information Convergence Engineering, Kyung Hee University, Yongin 17104, South Korea, and also with the Institute for Wearable Convergence Electronics, Kyung Hee University, Yongin 17104, South Korea (e-mail: sanghoek@khu.ac.kr).

Hyunwoo Kim and Kun-Woo Park are with the Department of Electronics and Information Convergence Engineering, Kyung Hee University, Yongin 17104, South Korea.

Jong-Han Kim is with the Department of Aerospace Engineering, Inha University, Incheon 22212, South Korea (e-mail: jonghank@inha.ac.kr).

Color versions of one or more figures in this article are available at <https://doi.org/10.1109/TMTT.2021.3106295>.

Digital Object Identifier 10.1109/TMTT.2021.3106295

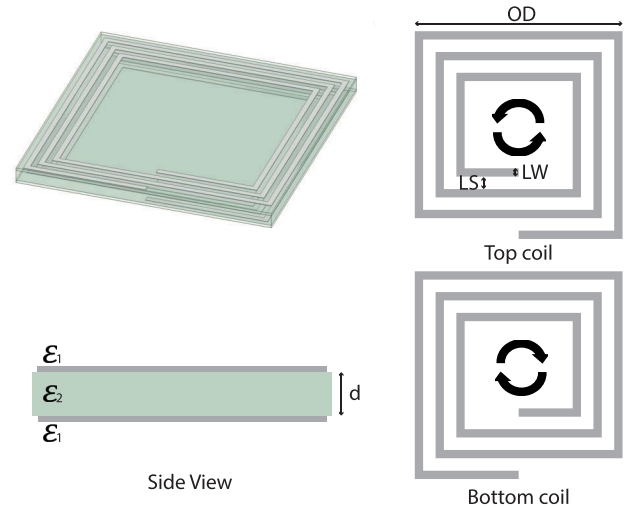


Fig. 1. Structure of a mirrored-coil LC sensor. The top coil and bottom coil rotate in different directions. In this work, the acronym OD, turns, LW, and LS stand for the outer diameter, the number of turns, the linewidth, and the line spacing, respectively.

lowers the resonant frequency of the sensor ω_s in which the information of pressure is encoded.

Among various LC-resonator structures, the mirrored-coil structure in Fig. 1 is a compelling candidate for biomedicine since it can be fabricated in the smallest dimension. This is because the mirrored-coil structure does not require a via, which hinders the sensor miniaturization due to its large footprint and requires additional fabrication steps [2]. The separation between two conductive coils by a dielectric medium forms the capacitance, which would resonate with the coil inductance at ω_s .

The key benefit of LC-resonator-based pressure sensor compared to other types of pressure sensors, such as resistive sensor [8], [9], lies in the easiness of wireless accessibility from outside the body. While the resistive sensor requires a complicated readout system, including an analog-to-digital converter and a separate communication module, the LC-resonator-based sensor inherently provides wireless access to its resonant frequency through the inductive coupling with an external reader.

There are many ways to access the resonant frequency from the reader. A traditional but still the most popular method is to

place the external reader of which the resonant frequency ω_1 is much higher than that of the sensor. The reader identifies the resonant frequency at which the electromagnetic (EM) energy is extracted particularly well by the resonance of the sensor. A drawback of this approach, however, is that the sensitivity and the sensing resolution are severely degraded when the Q -factor of the sensor is low and the coupling strength κ between the reader and the sensor is weak. Many studies have paved a way to overcome this limitation and improve sensing capabilities. For example, the idea of \mathcal{PTX} -symmetric telemetry [10] and multiple resonators locked to an exceptional point [11] was recently proposed.

While there have been intensive studies about how to wirelessly readout the resonant frequency of a miniaturized mirrored-coil sensor and its applications [1], [2], [4], [10]–[13], the study of the mirrored-coil sensor itself is poorly done relatively. To briefly review the analytical studies related to the passive sensor, the calculation of resonant frequency of split-ring resonators (SRRs) has been introduced in [14]–[16]. The case of more complicated structures such as multiturn coils, the data-fitted formula [17] for the inductance of a single planar coil is widely used to design both printed circuits and on-die inductors. Likewise, the parasitic capacitance of a planar coil can be computed through conformal mapping [18], [19]. However, the capacitance formed between two planar coils lacks studies for both analysis and design. As a result, investigators still utilize the most basic equation of the capacitance between two parallel plates; $C = \epsilon A/d$, where A and d refer to the overlap area of the coils and the separation between the plates, respectively [1], [2]. The prediction of the formula about the tendency between the capacitance and the separation is still valid, but the precision cannot be good since the coil structure is not a plate at all. The stray capacitance between the trace and the fringing field should be considered to be precise. Recently, there have been attempts to calculate the resonant frequency of two SRRs using coupled-mode theory (CMT) [20], which can be applied to compute that of the mirrored-coil structure in principle. However, the calculation process is semianalytical, which means that the calculation relies on preliminary field data computed from commercial field solvers. It prevents the users from quickly evaluating the sensor characteristics in the absence of commercial field solvers.

This work presents an analytical tool (Section II-A) and a data-fitted formula (Section II-B) about the resonant frequency of a mirrored-coil sensor of rectangular shape in Fig. 1. Although this work chooses the rectangular shape for the demonstration, our analytical method can be directly applied and the data-fitted formula can be similarly obtained for other shapes as well, such as circular, hexagonal, and octagonal coils. Those results are compared with the simulation results from the commercial field solver in Section III and with the measurement in Section IV. Both approaches show much better accuracy than the primitive formula, $C = \epsilon A/d$.

II. CALCULATION OF THE LC -RESONANT FREQUENCY

In this section, we propose two methods to calculate the resonant frequency of a mirrored-coil sensor. The analytical

method computes an effective inductance L and an effective capacitance C of the sensor using Green's operator and deduces the resonant frequency from them (Section II-A). Alternatively, to evaluate the resonant frequency even more conveniently, we propose a data-fitted formula numerically obtained from the results of field solvers in Section II-B.

A. Analytical Tool

The proposed analytical tool assumes the sinusoidal current over the coil and computes the resonant frequency depending on the coil structure and the dielectric property of the medium. At resonance of the lowest mode, the time-dependent current profile over the coil can be represented as $I_0 \cos(\pi x/l) \cos(\omega t)$, where l refers to the total length of the inductor when stretched into a straight line, x represents the coordinate variable such that it ranges between $-l/2$ and $l/2$, and ω represents the operating frequency in radian. From the charge conservation law ($\nabla \cdot \mathbf{J} = -(\partial \rho / \partial t)$), the time-dependent charge density profile can also be obtained as $\lambda_0 \sin(\pi x/l) \sin(\omega t)$ [21], where $\lambda_0 = \pi I_0 / (\omega l)$ is the maximum line charge density. From the EM theory [21], the effective inductance L and the effective capacitance C for a closed system can be defined as follows:

$$L = \frac{1}{|I_0|^2} \iint d\mathbf{r} d\mathbf{r}' \mathbf{J}(\mathbf{r}) \cdot \bar{\mathbf{G}}_A(\mathbf{r}, \mathbf{r}') \mathbf{J}(\mathbf{r}') \quad (1)$$

$$\frac{1}{C} = \frac{1}{|q_0|^2} \iint d\mathbf{r} d\mathbf{r}' \rho(\mathbf{r}) G_V(\mathbf{r}, \mathbf{r}') \rho(\mathbf{r}') \quad (2)$$

where $\bar{\mathbf{G}}_A$ (G_V) refers Green's operator on current (charge) density for the vector (scalar) potential \mathbf{A} (V) and q_0 refers the total amount of the charge ($q_0 = \lambda_0 l / \pi$) within the half of the coil ($0 \leq x \leq l/2$). With this approximation, the charge conservation law relates the reference current profile and the charge profile as $|I_0| = \omega |q_0|$. Although in [21] the integral was performed over a single coil, this work performs the integral over both coils and, hence, obtains the total inductance and capacitance of two mirrored coils. It should be noted that at resonance, magnetic induction from an external reader on the mirrored layout creates a standing current with the same magnitude but of opposite sign for the top and bottom coils (Fig. 1). This opposite distribution of charges creates higher capacitance than the case when the top and bottom inductors are rotating in the same directions, forming the fundamental resonant frequency of interests.

As defined, the resonant frequency is the frequency at which the average amount of the magnetic energy $L|I_0|^2/2$ and the electric energy $C|q_0|^2/2$ is equal. This yields the well-known equation of the resonant frequency

$$f_0 = \frac{1}{2\pi \sqrt{LC}}. \quad (3)$$

1) *LC Resonator in Homogeneous Media:* In a homogeneous medium of permittivity ϵ and a permeability μ , Green's

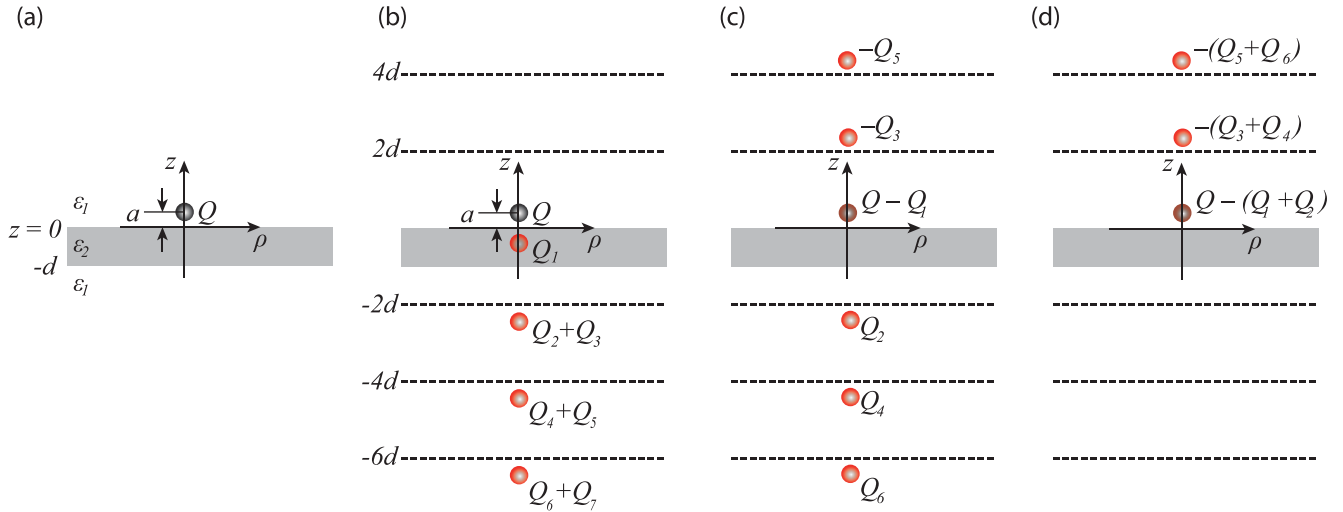


Fig. 2. Distribution of image charges to satisfy the boundary condition at $z = 0$ and $z = -d$. (a) Location of the unit charge. (b) Distribution of image charges for $z > 0$. (c) Distribution of image charges for $-d < z < 0$. (d) Distribution of image charges for $z < -d$.

operators for potentials act on the operands as

$$\tilde{\mathbf{G}}_{\mathbf{A}}(\mathbf{r}, \mathbf{r}') \mathbf{J}(\mathbf{r}') = \frac{\mu}{4\pi} \frac{\mathbf{J}(\mathbf{r}')}{|\mathbf{r} - \mathbf{r}'|} \quad (4)$$

$$G_V(\mathbf{r}, \mathbf{r}') \rho(\mathbf{r}') = \frac{1}{4\pi\epsilon} \frac{\rho(\mathbf{r}')}{|\mathbf{r} - \mathbf{r}'|} \quad (5)$$

resulting in the potentials from Biot–Savart’s law and Coulomb’s law, respectively. Although these simple operators are widely used for wireless antenna applications, they cannot analyze the resonating property of biomedical sensors. It is because the sensor substrate typically has a different electrical property from the surrounding tissue medium. The Green’s operators need to be modified to accommodate the in-homogeneity of media.

2) *LC Resonator in In-Homogeneously Layered Media:* Since the human body and most substrates on which the sensor is fabricated are nonmagnetic, the inductance L of the coil sensor can still be obtained from (1) and (4) or empirical findings [17]. In contrast, the permittivity largely differs between substrate and tissues, which necessitates the modification of Green’s operator for electric potential in (2).

Modeling the substrate in a medium as a planarly layered media as in Fig. 2(a), Green’s operator for the electric potential can be derived by the method of images [22]. The method of images can be applied to solve the fields in the presence of slab of ϵ_2 , as shown in Fig. 2(a). The boundary conditions are imposed at both interfaces of $z = 0$ and $z = -d$. Specifically, we have $\epsilon_1 E_{1,n} = \epsilon_2 E_{2,n}$, $E_{1,t} = E_{2,t}$, $\epsilon_2 E_{2,n} = \epsilon_1 E_{3,n}$, and $E_{2,t} = E_{3,t}$. The numerical indices in the subscripts refer to the fields in the region 1 ($z > 0$), the region 2 ($0 > z > -d$), and the region 3 ($z < -d$), and the subscripts n and t indicate the normal and the tangential component of the field to the interfacing surface, respectively.

To satisfy the boundary condition, an infinite number of image charges are required [23]. To represent the field and potential in the region 1, it can be shown that the image charges should be positioned as in Fig. 2(b), while for the fields and potentials in regions 2 and 3, the image charges

should locate as in Fig. 2(c) and (d). When z_n^m denotes the z coordinate of the n th image charge Q_n for the potential in the region m , the first few z_n^m is listed as follows:

$$\begin{aligned} z_1^1 &= -a, & z_2^1 &= z_3^1 = -2d - a, & z_4^1 &= z_5^1 = -4d - a \\ z_1^2 &= +a, & z_2^2 &= -2d - a, & z_3^2 &= 2d + a \\ z_1^3 &= z_2^3 = +a, & z_3^3 &= z_4^3 = 2d + a, & z_5^3 &= z_6^3 = 4d + a, \dots \end{aligned} \quad (6)$$

The locations of the image charges can be written in a general form as follows:

$$z_n^1 = \begin{cases} -(n-1)d - a, & \text{if } n \text{ is odd} \\ -nd - a, & \text{if } n \text{ is even} \end{cases} \quad (7)$$

$$z_n^2 = \begin{cases} (n-1)d + a, & \text{if } n \text{ is odd} \\ -nd - a, & \text{if } n \text{ is even} \end{cases} \quad (8)$$

$$z_n^3 = \begin{cases} (n-1)d + a, & \text{if } n \text{ is odd} \\ nd + a, & \text{if } n \text{ is even.} \end{cases} \quad (9)$$

The values of image charge Q_n can be determined by enforcing the boundary condition. For reference, the values of image charge Q_n and their corresponding location z_n^m in the z -coordinate are as follows:

$$Q_1 = \alpha_1 Q = \frac{\epsilon_1 - \epsilon_2}{\epsilon_1 + \epsilon_2} Q \quad (10)$$

$$Q_2 = \alpha_2 Q = \frac{-2\epsilon_2}{\epsilon_1 + \epsilon_2} Q_1 \quad (11)$$

$$Q_n = \alpha_n Q = \frac{\epsilon_1 - \epsilon_2}{\epsilon_1 + \epsilon_2} Q_{n-1}, \quad (\text{for } n \geq 3) \quad (12)$$

where α_n represents the ratio of the image charge Q_n to the original charge Q .

To solve the electric potential by the unit charge Q , the distribution of image charges can be chosen depending on the region of interest. For example, the potential in the region 1 ($z > 0$) by the charge Q at \mathbf{r}' (where $z' > 0$) can be expressed

as

$$V(\mathbf{r}; Q \text{ at } \mathbf{r}') = \frac{Q}{4\pi\epsilon_1} \left[\frac{1}{\sqrt{\rho^2 + (z-a)^2}} + \sum_{n=1}^{\infty} \frac{\alpha_n}{\sqrt{\rho^2 + (z-z_n^1)^2}} \right]. \quad (13)$$

Equation (2) implies that the electric energy stored is the summation of the product of charge and the electric potential at the position of the charge in the quasi-static approximation. For planar coils, all the charges are located on the surfaces of the substrate. To solve the potential at the position of charges, we may select either region interfacing the surface to compute the potential at the position of the charge. To incorporate the potentials at both interfaces of $z = 0$ and $-d$, we select the distribution of image charges for region 2 in Fig. 2(c) to compute the electric potential and energy stored in the system. Since $G_V(\mathbf{r}, \mathbf{r}') = V(\mathbf{r}; Q \text{ at } \mathbf{r}')/Q$, we have $G_V(\mathbf{r}, \mathbf{r}')$ of interests as

$$G_V(\mathbf{r}, \mathbf{r}') = \frac{1}{4\pi\epsilon_2} \left[\frac{1}{|\mathbf{r} - \mathbf{r}'|} + \sum_{n=1}^{\infty} \frac{(-1)^n \alpha_n}{|\mathbf{r} - \mathbf{r}_n'|} \right] \quad (14)$$

where \mathbf{r}_n' indicates the position of the n th image charge. Substituting this expression of Green's operator into (2) with the sinusoidal distribution of the discretized charges along the coil gives the capacitance. Specifically, for the numerical evaluation, the coils are first divided into N small line segments. The interval of each line segment is set as $\Delta l = 0.05$ mm, yielding $N = (\text{total coil length})/\Delta l$. The image charges are truncated when (14) converges at $n = 20$. Green's operator (14) is evaluated between every pair of the line segments, yielding an $N \times N$ matrix. The integration of (2) is performed by summing up the matrix multiplied with the corresponding charge distributions, giving the capacitance. Last, one can obtain the resonant frequency of the mirrored coil by (3). Since the permittivity of the substrate affects the magnitude of image charges as (10)–(12) and the substrate height does the distance between the pair of the segments in (14), the substrate properties affect the resonant frequency.

The benefits of the proposed analytical tool are manifold. First, the method is freely available to users through the open codes [24], [25], while most finite element methods (FEM) and finite-difference time-domain (FDTD) methods are only available through licensed software, such as Ansys HFSS and Simulia CST. Second, the resonant frequency of the mirrored coils can be evaluated much faster than the FEM and the FDTD since it does not need to construct meshes for the media [26], [27]. Last, the analytical method is also valuable since it provides physical insights. For example, for the mirrored-coil structure, the opposite distribution of charges creates strong electric fields between the top and bottom coils, which dominantly decides the capacitance of the closed system. On the other hand, if the top and bottom inductors are rotating in the same direction, the electric fields between the coils are weak and the stray capacitance between the adjacent turns in each coil dominates the effective capacitance. Therefore, for the pressure sensor application, the coils should be placed in the mirrored manner to react sensitively to the

interlayer condition change [1], [2], [4], [10]–[13]. This is a physical insight that cannot be inferred from the primitive formula, $C = \epsilon A/d$, empirical models, or the blind use of commercial EM solvers.

B. Data-Fitted Formula

The above analytical method provides physical insights into how the mirrored coil behaves at resonance. On the other hand, it is often convenient to calculate the resonant frequency with a data-fitted formula. The data-fitted formula expresses the resonant frequency as a closed-form function of physical parameters. Therefore, it also helps changes in the resonant frequency being quantitatively mapped to the changes of physical parameters, such as dielectric permittivity of the surrounding medium or the separation between the coils. In this section, we build an empirical data-fitted formula for the resonance frequency of planar mirrored-coil sensors. We collected 1070 data samples from a commercial FEM field solver (Ansys HFSS [28]) results, among which 603 ($=n_{\text{train}}$) samples are used for training and the rest for validation. The samples have six input features, where each parameter is simulated in the following range. A number of turns are varied between 2 and 4, relative outside permittivity is varied between 1 and 50, line spacing (LS) and linewidth (LW) are varied between 0.1 and 0.3 mm, the distance between the plates is varied between 0.3 and 0.6 mm, relative substrate permittivity is varied between 2.2 and 8.8, and the outer diameter (OD) is varied between 2 and 8 mm. These values were chosen based on dimensions of LC sensors for implantable purposes [1], [2], [4], [10], [11], [13]. Then, the six input features, x_1, \dots, x_6 , were scaled by their maximum range in the training dataset so that they do not exceed unity.

- 1) x_1 : Number of turns, scaled by 1/4.
- 2) x_2 : Relative permittivity of outside material, scaled by 1/50.
- 3) x_3 : LS and LW in mm, scaled by 1/0.3.
- 4) x_4 : Substrate thickness in mm, scaled by 1/0.6.
- 5) x_5 : Relative permittivity of substrate material, scaled by 1/8.
- 6) x_6 : Outer diameter in mm, scaled by 1/32.

The output feature of the samples, y , is the resonant frequency in gigahertz, which we assume to be related by the product of a monomial function and exponential functions of the input features. This leads to the following prediction model:

$$\hat{y} = e^b \prod_{i=1}^6 x_i^{\theta_i} e^{\beta_i x_i} \quad (15)$$

where \hat{y} is the predicted resonant frequency in gigahertz and $b, \theta_1, \beta_1, \dots, \theta_6, \beta_6$ are the predictor parameters that we will find. Taking the logarithm and denoting the sample number in the superscript with the parentheses gives

$$\log \hat{y}^{(k)} = b + \sum_{i=1}^6 \left(\theta_i \log x_i^{(k)} + \beta_i x_i^{(k)} \right) \quad (16)$$

which implies that the logarithm of the predicted frequency is linear in the predictor parameters. For example, $x_1^{(k)}$ implies

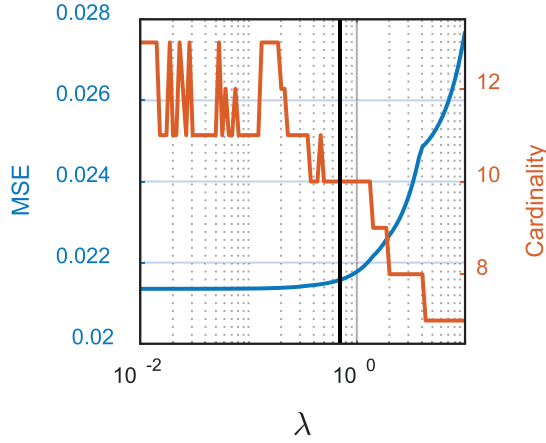


Fig. 3. Regularization path for optimal MSE and the cardinality of the predictor parameter.

the number of turns (scaled by 4) of the k th LC sensor from the dataset, and $\hat{y}^{(k)}$ represents the predicted resonant frequency for the k th sample, computed by our predictor.

Now, we define the following loss function describing the model fitness over the train set:

$$\mathcal{L}(b, \theta_1, \beta_1, \dots, \theta_6, \beta_6) = \sum_{k=1}^{n_{\text{train}}} (\log \hat{y}^{(k)} - \log y^{(k)})^2 \quad (17)$$

with the ℓ_1 regularizer promoting sparsity in the predictor parameters

$$r(\theta_1, \beta_1, \dots, \theta_6, \beta_6) = \sum_{i=1}^6 (|\theta_i| + |\beta_i|). \quad (18)$$

Then, we find the optimal predictor parameters fitting the train set by solving the following least absolute shrinkage and selection operator (LASSO)-type problem [29] with a nonnegative weighting parameter λ :

$$\min_{b, \theta_1, \beta_1, \dots} \mathcal{L}(b, \theta_1, \beta_1, \dots) + \lambda r(\theta_1, \beta_1, \dots). \quad (19)$$

The LASSO model was used since it is suitable for systematically revealing the dominant features from the candidate input features, thus resulting in simple model structures (see Fig. 3). Finding simple data-fitted models at the cost of accuracy loss is desirable since they provide valuable insights into the sensitivity of the input features. Typical LASSO design procedures can be found, for example in Chapter 3.4 of [29]. Note that they can be easily handled by general off-the-shelf convex optimization solvers, such as *cvxpy* [30].

Fig. 3 shows the optimal mean squared error (MSE) = $\mathcal{L}^*/n_{\text{train}}$ and the cardinality of $b, \theta_1, \beta_1, \dots, \theta_6, \beta_6$ for $0.01 \leq \lambda \leq 10$. From this regularization path, we choose $\lambda = 0.7$ (the vertical black line) since it simplifies the model by sufficiently reducing the cardinality while increasing the MSE no more than 2% from its attainable minimum. We present the empirical formula obtained from $\lambda = 0.7$ in the following:

$$\hat{y} = 0.02490 \frac{1.069^{x_2} 0.8181^{x_5} 1.399^{x_6} x_3^{0.2260} x_4^{0.1603}}{x_1^{1.131} x_2^{0.1110} x_5^{0.2165} x_6^{1.553}}. \quad (20)$$

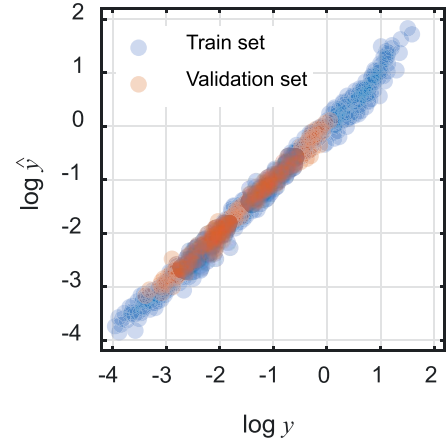


Fig. 4. Prediction accuracy of the empirical model, $\log \hat{y}$ versus $\log y$.

TABLE I

MSE AND PERCENTAGE ERROR OF THE EMPIRICAL MODEL

	MSE	RMSE	Percentage error
Train set	0.02157	0.1469	15.8%
Validation set	0.01354	0.1164	12.3%

The prediction accuracy is assessed in Fig. 4 and Table I. The prediction and the ground-truth resonant frequency from the dataset are plotted in Fig. 4, where the blue dots and the orange dots represent sample points from the train set and the validation set, respectively.

It is worth noting that this work chose to express the resonant frequency with a formula instead of effective inductance and capacitance since, in biomedicine, the resonant frequency is of main interest. In case that one is interested in the expression of the effective inductance of a planar coil, one may refer to [17]. Since most materials used for biomedicine are nonmagnetic, the formula can be readily used to compute the inductance for the LC sensor. This formula along with the proposed formula for the resonant frequency in this work can yield the expression for the capacitance as well.

III. COMPARISON TO FIELD SOLVERS

To validate our calculations in Section II, we simulate LC resonators using the FEM field solver [28]. A single-turn coil with a comparable size to mirrored coils is chosen as an external reader so that it resonates at a higher frequency than the mirrored coils. Then, the external reader is placed 5 mm above the mirrored coils. The resonant frequency of the mirrored coil is the frequency at which the maximum power reflection distortion occurs [2].

Fig. 5 shows the analytical calculation results compared with the FEM results. The solid line (dashed line) indicates the analytical calculation (data-fitted formula) results, whereas the asterisk markers indicate the values obtained from the FEM. The values are compared for various parameters of OD, the number of turns, and the dielectric constant of the substrate, while the LW and LS are fixed to 0.5 mm. In Fig. 5(c) and (d) where the sensor is inside the muscle, the relative permittivity of the muscle is set as 50 assuming a low-gigahertz frequency [31], while the dielectric loss is ignored. For all the parameters listed above, the results show

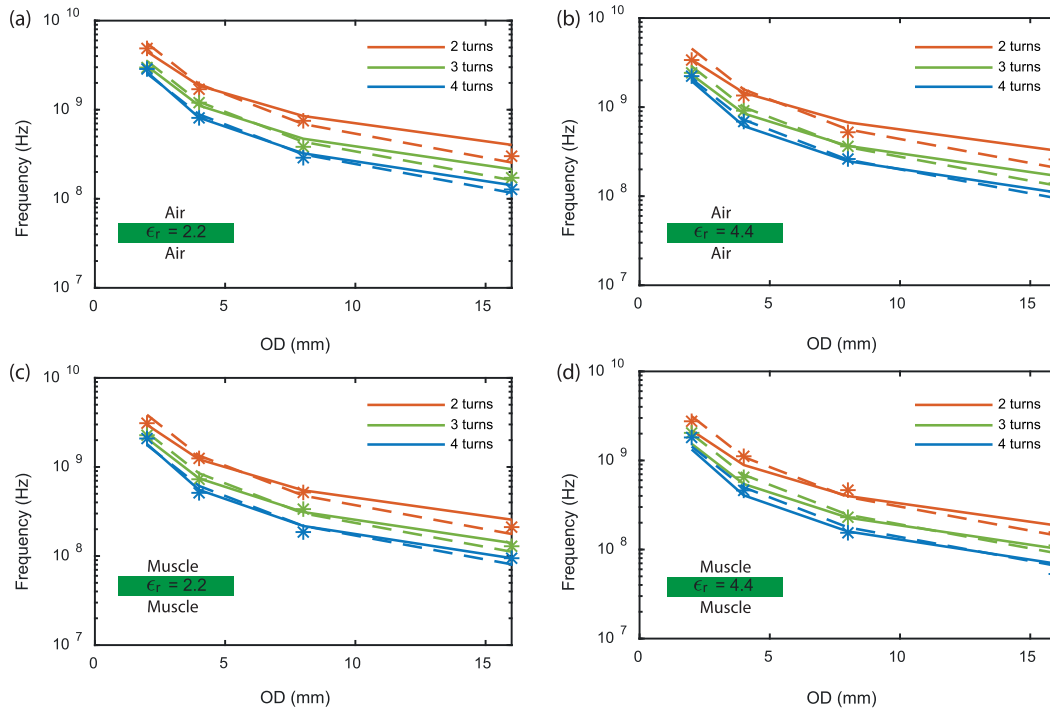


Fig. 5. Plot of resonant frequency for various coil parameters. Solid line indicates analytical calculations, dashed line indicates calculations using data-fitted formula, and markers represent the results from FEM. The parameters for each subplot are as follows. (a) $\epsilon_r = 2.2$, in air. (b) $\epsilon_r = 4.4$, in air. (c) $\epsilon_r = 2.2$, in muscle ($\epsilon_{r,\text{muscle}} = 50$). (d) $\epsilon_r = 4.4$, in muscle ($\epsilon_{r,\text{muscle}} = 50$).

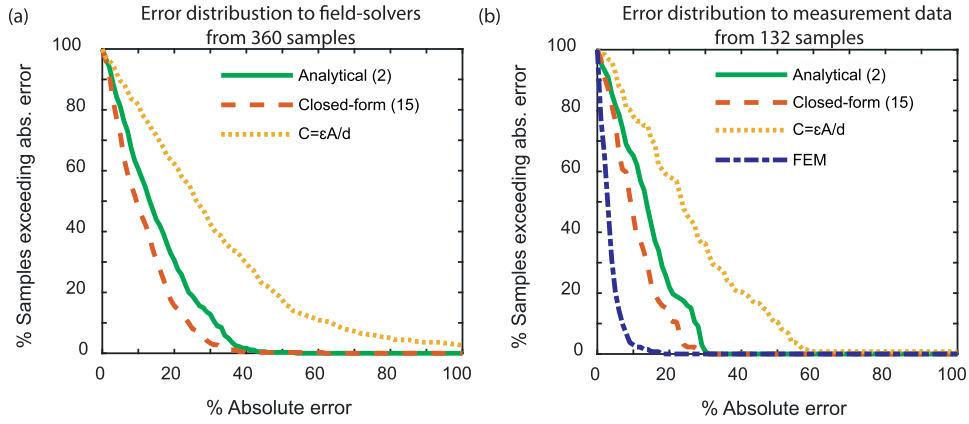


Fig. 6. Error distributions for (a) analytical calculations (solid line), data-fitted formula calculations (dashed line), and the primitive calculations (dotted line) compared to field solvers and (b) analytical calculations (solid line), data-fitted formula calculations (dashed line), primitive calculations (dotted line), and FEM simulations (dashed and dotted line) compared to measurement results.

TABLE II

COMPARISON OF MEDIAN ERROR FOR VARIOUS CALCULATION METHODS

	Analytical	Data-fitted	$C=\epsilon A/d$
Median Error from FEM	12 %	8%	26%
Median Error from Measurement	13%	9%	23%

a good agreement between analytical calculations and FEM results.

To further quantify the accuracy of the proposed methods, we use the absolute percentage error to analyze the accuracy of analytical calculations. The error distribution is obtained from 360 samples where the number of turns is varied between 2 and 4, OD is varied between 2 and 8 mm, relative permittivity

is varied between 2.2 and 8.8, the relative permittivity of the surrounding material is varied between 1 and 50, and the LW and LS are varied between 0.1 and 0.3 mm. These values are selected based on dimensions of *LC* sensors for implantable purposes [1], [2], [4], [10], [11], [13]. The absolute percentage error is obtained as $100|f_{\text{calc}} - f_{\text{FEM}}|/f_{\text{FEM}}$. This corresponds to the *x*-axis of Fig. 6(a). The *y*-axis of Fig. 6(a) indicates the percentage of samples that exceed the specified absolute error.

Fig. 6(a) shows the error distributions of analytical calculation, data-fitted formula calculation, and primitive calculation results compared to FEM simulation results. The primitive calculation is obtained by calculating the capacitance as $C = \epsilon_2(A/d)$, where *A* is the intersecting area between the top and bottom coils.

TABLE III
INDUCTOR PARAMETERS USED FOR EXPERIMENTS AND COMPARISON TO CALCULATIONS AND FIELD SOLVERS

Turns	ϵ_{r1}	LW/LS (mm)	d (mm)	ϵ_{r2}	OD (mm)	FEM (GHz)	Analytic (GHz)	Formula (GHz)	Measurement (GHz)
3	80	0.4	0.6	3.9	6	0.76121	0.64423	0.58998	0.68707
3	1	0.2	0.5	3.9	8	0.5133	0.4569	0.46844	0.51272
3	80	0.1	0.6	3.9	4	0.83717	0.6081	0.79274	0.8644
3	1	0.3	0.3	3.9	8	0.48207	0.4913	0.47303	0.478
3	80	0.2	0.6	3.9	8	0.33434	0.2943	0.32953	0.34733
3	50	0.2	0.6	3.9	4	1.066	0.8404	0.9385	1.027
3	50	0.1	0.5	3.9	6	0.47752	0.36	0.42399	0.4887
3	1	0.2	0.3	3.9	8	0.44919	0.4343	0.43161	0.45053
3	50	0.1	0.6	3.9	6	0.48742	0.36642	0.43656	0.499
3	80	0.2	0.6	3.9	6	0.5357	0.4379	0.50444	0.5284
3	50	0.3	0.5	3.9	4	1.3705	1.1177	0.99893	1.293
3	80	0.4	0.3	3.9	6	0.6159	0.58797	0.52794	0.60867
3	1	0.1	0.3	3.9	8	0.4234	0.383	0.36903	0.43181
3	50	0.2	0.5	3.9	8	0.32455	0.2951	0.32394	0.33813
3	50	0.3	0.5	3.9	8	0.36758	0.3382	0.35503	0.35587
3	50	0.4	0.3	3.9	8	0.35631	0.36424	0.34909	0.35333
3	1	0.3	0.5	3.9	4	2.004	1.6777	1.4445	2.0454
3	50	0.2	0.5	3.9	6	0.52859	0.4386	0.49589	0.51547
3	1	0.1	0.6	3.9	4	1.1576	0.95421	1.1603	1.2237
3	1	0.1	0.4	3.9	8	0.44747	0.392	0.38645	0.45717
3	80	0.3	0.5	3.9	4	1.2939	1.0895	0.98688	1.2825
3	50	0.1	0.5	3.9	8	0.3133	0.2529	0.27697	0.33687
3	50	0.1	0.6	3.9	4	0.86727	0.62246	0.80242	0.8733
3	50	0.1	0.3	3.9	6	0.44657	0.34077	0.39065	0.461
3	80	0.2	0.3	3.9	4	0.8899	0.74345	0.82967	0.9232
3	80	0.3	0.4	3.9	4	1.2482	1.056	0.95221	1.2415
3	1	0.3	0.5	3.9	6	0.8715	0.8011	0.7859	0.9025
3	1	0.2	0.5	3.9	6	0.7479	0.6716	0.71709	0.78022
3	50	0.1	0.6	3.9	8	0.32747	0.2571	0.28519	0.34573
3	80	0.3	0.3	3.9	4	1.1367	1.0144	0.90929	1.1827
3	50	0.1	0.4	3.9	8	0.31101	0.24753	0.26724	0.328
3	80	0.3	0.5	3.9	6	0.5884	0.5155	0.53692	0.5732
3	80	0.1	0.3	3.9	6	0.4387	0.33286	0.38594	0.46307
3	50	0.1	0.4	3.9	6	0.46556	0.3518	0.40909	0.48
3	50	0.3	0.4	3.9	6	0.55505	0.5134	0.52438	0.55473
3	1	0.4	0.6	3.9	6	1.1266	0.99461	0.86357	1.1374
3	50	0.3	0.5	3.9	6	0.6005	0.5287	0.54348	0.57373
3	1	0.3	0.6	3.9	4	2.1102	1.7177	1.4874	2.1372
3	1	0.3	0.6	3.9	8	0.57626	0.5282	0.52862	0.57944
3	80	0.4	0.4	3.9	8	0.3703	0.36813	0.36116	0.3716
3	80	0.2	0.4	3.9	6	0.48434	0.4159	0.47269	0.49947
3	50	0.3	0.3	3.9	4	1.1842	1.0412	0.9204	1.193
3	50	0.4	0.3	3.9	6	0.63121	0.60346	0.53439	0.61173
3	50	0.1	0.3	3.9	4	0.7685	0.5741	0.71803	0.7967
3	1	0.3	0.6	3.9	6	0.9214	0.8187	0.80921	0.94386
3	1	0.4	0.4	3.9	8	0.57152	0.57715	0.52863	0.5785
3	50	0.2	0.3	3.9	8	0.31202	0.2776	0.29847	0.3128
3	1	0.1	0.4	3.9	4	1.0774	0.9175	1.0873	1.1515
3	50	0.3	0.6	3.9	8	0.3917	0.3459	0.36556	0.36347
3	1	0.1	0.6	3.9	8	0.47979	0.40332	0.4124	0.48917
3	50	0.2	0.3	3.9	6	0.4769	0.41084	0.4569	0.47747
3	80	0.1	0.3	3.9	4	0.7471	0.5605	0.70937	0.79627
3	80	0.2	0.3	3.9	8	0.30455	0.2708	0.29487	0.31467
3	1	0.2	0.6	3.9	4	1.536	1.2667	1.3571	1.5685
3	80	0.1	0.4	3.9	8	0.3053	0.2419	0.26402	0.3296
3	1	0.3	0.5	3.9	8	0.56182	0.5179	0.5134	0.55892
3	1	0.1	0.5	3.9	4	1.098	0.9381	1.1269	1.1893
3	1	0.1	0.3	3.9	4	1.0455	0.8899	1.0383	1.0725
3	80	0.2	0.4	3.9	8	0.3209	0.28048	0.30879	0.32773
3	1	0.2	0.4	3.9	4	1.3848	1.2014	1.2717	1.4257

The median error is defined as the error crossing the horizontal line at the 50% level [17]. Fig. 6(a) shows that the error distribution for analytical calculations and data-fitted formula and the median error compared to field solvers are assessed in Table II. The median error results in 12% and 8%,

respectively, which is significantly smaller than the primitive calculation of 26%. In the case of the analytical formula, the error mainly originates from the discrepancy between the actual charge distribution and the sinusoidal form assumed in the calculation.

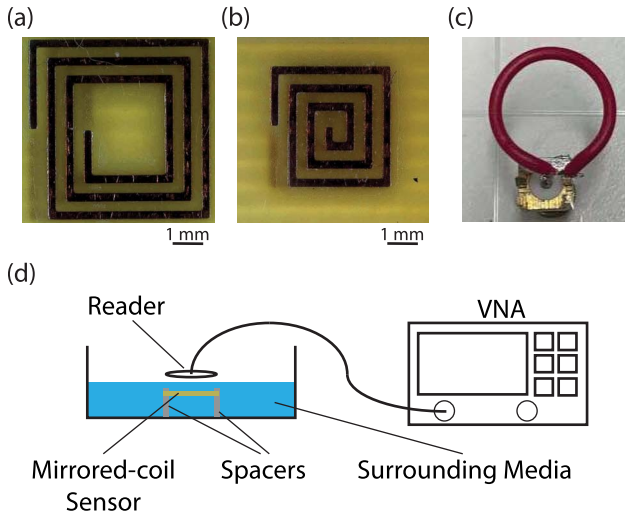


Fig. 7. Fabricated LC sensor with (a) 6-mm diameter and (b) 4-mm diameter. (c) External reader for measurement. (d) Illustration of the experiment setup.

IV. MEASUREMENT RESULTS

We fabricate LC resonators on an FR-4 board using standard printed circuit board (PCB) technology and measure the resonant frequency for 132 different parameters. Selected set of parameters for measurement is presented in Table III and the resonators of OD of 6 and 4 mm are shown in Fig. 7(a) and (b), respectively. The measurement is performed in air, freshwater, and an ethanol–water mixture that mimics the permittivity to the human muscle in the microwave regime [31]. Four pillars are placed at each corner of the LC resonator so that the external material completely surrounds the LC sensor. Then, a single-coil reader with a radius of 7 mm as shown in Fig. 7(c) is placed above the LC resonator. The resonant frequency is measured by the maximum power reflection distortion using a vector network analyzer (Rohde and Schwarz ZNLE6), as shown in Fig. 7(d).

Fig. 6(b) shows the error distribution of analytical, data-fitted formula, primitive calculations, and FEM simulation results. The error distribution exhibits the absolute percentage error from the measurement results. Also, the median error obtained from the error distribution is assessed in Table II. The results show that FEM simulations have the least error of less than 3% since it considers every detailed aspect of the mirrored-coil sensor. For instance, the thickness of the copper layer or the thin organic solderability preservative (OSP) layer that goes on top of the copper layer to prevent the copper from oxidation. On the other hand, the primitive calculation results had the highest error of 23% since it does not consider stray or fringing capacitance. Finally, analytical calculations and data-fitted formula calculations resulted in a median error of 13% and 9%, respectively, showing much better accuracy than the primitive calculation.

V. CONCLUSION

This work offers two different methods for calculating the resonant frequency of planar mirrored-coil sensors for biomedical applications. The first (analytical calculation) method

is based on an assumption that the charge profile at the lowest mode is well approximated by a sinusoidal function. Green's operator accommodating the dielectric permittivity of the outside material and substrate is deduced by the method of images. By applying Green's operators to the source profiles, we calculate the effective inductance and capacitance from which one can obtain the resonant frequency. The second (data-fitted formula) method solves the LASSO type problem, assuming that the resonant frequency is the product of a monomial function and exponential functions of the coil parameters.

For both methods, the calculation results agree well with results from a field solver with a median error of 12% (8%) for analytical calculations (data-fitted formulas). The results are also compared to measurement results where the median error results in 13% (9%) for analytical calculations (data-fitted formulas). Engineers can use these methods to quickly evaluate and design the mirrored-coil structure with high precision.

REFERENCES

- [1] C. M. Boutry *et al.*, "Biodegradable and flexible arterial-pulse sensor for the wireless monitoring of blood flow," *Nature Biomed. Eng.*, vol. 3, no. 1, pp. 47–57, Jan. 2019.
- [2] L. Y. Chen *et al.*, "Continuous wireless pressure monitoring and mapping with ultra-small passive sensors for health monitoring and critical care," *Nature Commun.*, vol. 5, no. 1, pp. 1–10, Dec. 2014.
- [3] G. Chitnis, T. Maleki, B. Samuels, L. B. Cantor, and B. Ziaie, "A minimally invasive implantable wireless pressure sensor for continuous IOP monitoring," *IEEE Trans. Biomed. Eng.*, vol. 60, no. 1, pp. 250–256, Jan. 2013.
- [4] P.-J. Chen, D. C. Rodger, S. Saati, M. S. Humayun, and Y.-C. Tai, "Microfabricated implantable parylene-based wireless passive intraocular pressure sensors," *J. Microelectromech. Syst.*, vol. 17, no. 6, pp. 1342–1351, Dec. 2008.
- [5] P.-J. Chen, S. Saati, R. Varma, M. S. Humayun, and Y.-C. Tai, "Wireless intraocular pressure sensing using microfabricated minimally invasive flexible-coiled LC sensor implant," *J. Microelectromech. Syst.*, vol. 19, no. 4, pp. 721–734, Aug. 2010.
- [6] S.-Y. Wu, C. Yang, W. Hsu, and L. Lin, "3D-printed microelectronics for integrated circuitry and passive wireless sensors," *Microsyst. Nanoeng.*, vol. 1, no. 1, pp. 1–9, Dec. 2015.
- [7] J. Melgaard, J. J. Struijk, and N. J. M. Rijkhoff, "Minimizing a wireless passive LC -tank sensor to monitor bladder pressure: A simulation study," *J. Med. Biol. Eng.*, vol. 37, no. 6, pp. 800–809, Dec. 2017.
- [8] D. Kang *et al.*, "Ultrasensitive mechanical crack-based sensor inspired by the spider sensory system," *Nature*, vol. 516, pp. 222–226, Dec. 2014.
- [9] T. Yamada *et al.*, "A stretchable carbon nanotube strain sensor for human-motion detection," *Nature Nanotechnol.*, vol. 6, no. 5, p. 296, 2011.
- [10] P.-Y. Chen *et al.*, "Generalized parity–time symmetry condition for enhanced sensor telemetry," *Nat. Electron.*, vol. 1, pp. 297–304, May 2018.
- [11] Z. Dong, Z. Li, F. Yang, C.-W. Qiu, and J. S. Ho, "Sensitive read-out of implantable microsensors using a wireless system locked to an exceptional point," *Nature Electron.*, vol. 2, no. 8, pp. 335–342, Aug. 2019.
- [12] L. Y. Chen *et al.*, "Mass fabrication and delivery of 3D multilayer μ tags into living cells," *Sci. Rep.*, vol. 3, no. 1, pp. 1–6, Dec. 2013.
- [13] X. Hu *et al.*, "Micrometer-scale magnetic-resonance-coupled radio-frequency identification and transceivers for wireless sensors in cells," *Phys. Rev. A, Gen. Phys.*, vol. 8, no. 1, Jul. 2017, Art. no. 014031.
- [14] J. Y. Siddiqui, C. Saha, C. Sarkar, L. A. Shaik, and Y. M. M. Antar, "Ultra-wideband antipodal tapered slot antenna with integrated frequency-notch characteristics," *IEEE Trans. Antennas Propag.*, vol. 66, no. 3, pp. 1534–1539, Mar. 2018.
- [15] C. Saha and J. Y. Siddiqui, "A comparative analysis for split ring resonators of different geometrical shapes," in *Proc. IEEE Appl. Electromagn. Conf. (AEMC)*, Dec. 2011, pp. 1–4.

- [16] C. Saha and J. Y. Siddiqui, "Versatile CAD formulation for estimation of the resonant frequency and magnetic polarizability of circular split ring resonators," *Int. J. RF Microw. Comput.-Aided Eng.*, vol. 21, no. 4, pp. 432–438, Jul. 2011.
- [17] S. S. Mohan, M. del Mar Hershenson, S. P. Boyd, and T. H. Lee, "Simple accurate expressions for planar spiral inductances," *IEEE J. Solid-State Circuits*, vol. 34, no. 10, pp. 1419–1424, Oct. 1999.
- [18] X. Jin, Q. Wang, W. Q. Khan, Z. H. Tang, and X. M. Yao, "Analytical computation of distributed capacitance for NFC coil antenna," *IEICE Electron. Exp.*, vol. 14, no. 2, 2017, Art. no. 20161147.
- [19] U.-M. Jow and M. Ghovanloo, "Modeling and optimization of printed spiral coils in air, saline, and muscle tissue environments," *IEEE Trans. Biomed. Circuits Syst.*, vol. 3, no. 5, pp. 339–347, Oct. 2009.
- [20] S. Y. Elnaggar, R. J. Tervo, and S. M. Mattar, "Energy coupled mode theory for electromagnetic resonators," *IEEE Trans. Microw. Theory Techn.*, vol. 63, no. 7, pp. 2115–2123, Jul. 2015.
- [21] A. Kurs, A. Karalis, R. Moffatt, J. D. Joannopoulos, P. Fisher, and M. Soljačić, "Wireless power transfer via strongly coupled magnetic resonances," *Science*, vol. 317, no. 5834, pp. 83–86, 2007.
- [22] J. D. Jackson, *Classical Electrodynamics*. Hoboken, NJ, USA: Wiley, 2007.
- [23] T. Sometani, "Image method for a dielectric plate and a point charge," *Eur. J. Phys.*, vol. 21, no. 6, p. 549, 2000.
- [24] A. E. Lab. (2021). *Analytical Calculation of Mirrored Coil Resonators*. [Online]. Available: github.com/jonghunkhu/mirrored-coil-analytical
- [25] A. E. Lab. (2021). *Data-Fitted Formula for Mirrored Coil Resonators*. [Online]. Available: github.com/aisl-khu/HFSS-train/tree/master/via_cvx
- [26] J.-M. Jin, *The Finite Element Method in Electromagnetics*. Hoboken, NJ, USA: Wiley, 2015.
- [27] A. Taflov and S. C. Hagness, *Computational Electrodynamics: The Finite-Difference Time-Domain Method*. Norwood, MA, USA: Artech House, 2005.
- [28] *HFSS*, Ansys Inc., Canonsburg, PA, USA, 1998, vol. 15317.
- [29] J. Friedman, T. Hastie, and R. Tibshirani, *The Elements of Statistical Learning* (Springer Series in Statistics), vol. 1, no. 10. New York, NY, USA: Springer, 2001.
- [30] S. Diamond and S. Boyd, "CVXPY: A Python-embedded modeling language for convex optimization," *J. Mach. Learn. Res.*, vol. 17, no. 83, pp. 1–5, 2016.
- [31] S. Gabriel, R. W. Lau, and C. Gabriel, "The dielectric properties of biological tissues: III. Parametric models for the dielectric spectrum of tissues," *Phys. Med. Biol.*, vol. 41, no. 11, p. 2271, 1996.



Jongheon Lee received the B.S. and M.S. degrees in electronic engineering from Kyung Hee University, Yongin, South Korea, in 2019 and 2021, respectively.

His research focuses on the applications of radio frequency technology and electromagnetic theory in wireless power transfer for industrial and biomedical applications.



Hyunwoo Kim (Student Member, IEEE) was born in Daejeon, South Korea, in 1997. He is currently pursuing the B.S. degree in electronic engineering at Kyung Hee University, Yongin, South Korea.

His research interests include wireless power transfer and wireless implantable biomedical systems.



Kun-Woo Park was born in Goyang, South Korea, in 1997. He received the B.S. degree in electronic engineering and the M.S. degree in electronic information convergence engineering from Kyung Hee University, Yongin, South Korea, in 2020 and 2021, respectively.

He is currently an AI Researcher with AI Lab, Deltax Company, Ltd., Seoul, South Korea. His research has been concerned with application of deep learning and deep reinforcement learning.



Jong-Han Kim received the B.S. and M.S. degrees in aerospace engineering from Korea Advanced Institute of Science and Technology (KAIST), Daejeon, South Korea, in 1999 and 2001, respectively, and the Ph.D. degree in aeronautics and astronautics from Stanford University, Stanford, CA, USA, in 2012.

He was an Assistant Professor with the Department of Electronic Engineering, Kyung Hee University, Yongin, South Korea. Prior to that, he was a Senior Researcher with the Agency for Defense Development (ADD), Daejeon, being in charge of developing guidance and control techniques for missile systems development programs. He is currently an Assistant Professor with the Department of Aerospace Engineering, Inha University, Incheon, South Korea. His research interests include advanced optimization techniques, inference and learning, and aerospace applications of advanced guidance and control techniques.



Sanghoek Kim (Member, IEEE) received the B.S. degree in electrical engineering and mathematics from Seoul National University, Seoul, South Korea, in 2007, and the M.S. and Ph.D. degrees in electrical engineering from Stanford University, Stanford, CA, USA, in 2011 and 2013, respectively.

He worked with Qualcomm Inc., San Diego, CA, as a Signal/Power Integrity Engineer and SiBeam Inc., Sunnyvale, CA, as a mmWave System Engineer. In 2016, he joined the Department of Electrical Engineering, Kyung Hee University, Yongin, South Korea, as an Assistant Professor. His current research focuses on the applications of radio frequency technology and electromagnetic theory in wireless interface with bio-implantable devices, biomedicine, wireless power transfer, and radar technologies.

Dr. Kim was a recipient of Kwanjeong Scholarship during the study.